

DeepLab: 基于深度卷积网络、空洞卷积、全连接条件随机场的图像语义分割方法

Liang-Chieh Chen, George Papandreou, Senior Member, IEEE, Iasonas Kokkinos, Member, IEEE, Kevin Murphy, and Alan L. Yuille, Fellow, IEEE

译者：林会东 学号：201636665056

Abstract—在本项目中，我们使用深度学习解决了图像语义分割问题，并做出了三个主要的贡献，且通过实验证明了它们具有重要的、实质性的实用价值。首先，我们使用上采样滤波器（或空洞卷积）作为密集预测任务中的重要工具。空洞卷积允许我们明确地控制在深度卷积神经网络中计算特征响应的分辨率，同时它还允许我们有效地扩大滤波器的视野以结合更大的输入背景而不增加参数的数量或计算量。其次，我们建议使用空洞空间金字塔池化层（ASPP），支持以多个不同的尺度大小对输入图片进行分割，鲁棒性更好。ASPP 使用多尺度、多采样率的感受野对输入卷积层进行滤波处理，从而支持捕获多个尺度下的物体及图像上下文。第三，我们通过结合 DCNN 和概率图形模型的方法来改进对象边界的定位。DCNN 中通常使用的最大池化和下采样的组合实现了不变性，但是它们对精度有影响，于是我们将 DCNN 的最后一层响应与全连接的条件随机场（CRF）相连来克服这一缺陷。CRF 在定位精度问题上在定性与定量方面均有着优异的优化效果。我们提出的 DeepLab 系统在 PASCAL VOC-2012 图像语义分割任务中以 79.7% 的 mIoU 斩获新高，同时也提升了 PASCAL-Context, PASCAL-Person-Part, and Cityscapes 这三项数据集的结果。我们的所有代码均开源。

Index Terms—卷积神经网络, 语义分割, 空洞卷积, 条件随机场

1 Introduction

深度卷积神经网络（DCNNs）[1] 已经将计算机视觉系统在各种高级问题上的性能推向了历史新高，包括图像分类 [2], [3], [4], [5], [6] 和对象检测 [7], [8], [9], [10], [11], [12]，其中 DCNNs 以端到端训练的方式完胜传统的人工特征提取，取得了惊人的效果。

DCNNs 成功的关键在于它们对局部图像变换的内置不变性，这使它们能够学习越来越抽象的数据表示 [13]。这种不变性对于分类任务显然是可取的，但是对于像素级敏感的、密集的预测任务不尽然，例如语义分割，其中空间信息的抽象是不希望看到的。

特别地，我们考虑将 DCNNs 应用于图像语义分割任务中的以下三个挑战：(1) 降低的特征分辨率，(2) 存在多尺度变化下的物体，以及 (3) 由于 DCNNs 不变性而导致的定位精度下降。接下来，我们将讨论这些挑战及在我们提出的 DeepLab 系统中克服它们的方法。

第一个挑战是由最初为图像分类设计的多级最大池化及下采样（stride）操作组合引起的 [2], [4], [5]。当 DCNNs 以完全卷积方式计算时，计算出的特征图的分辨率显著下降 [14]。为了克服这一障碍并有效生成更为密集的特征，我们从 DCNNs 的最后几个最大池化层中移除了下采样操作，并在后续的卷积层中使用上采样滤波器，从而以更高的采样率计算特征。上采样滤波器相当于在非零滤波器的感受野中插入了许多空洞。这项技术在信号处理领域有着悠久的历史，最初是用来计算小波变换的 [15]。我们借用了术语“空洞卷积”作为使用上采样滤波器卷积的缩写。已经有不少 DCNNs 曾使用了这一技术并发表了文章 [3], [6], [16]。在实践中，我们通过结合空洞卷积来恢复全分辨率特征图，这种卷积方法更加密集地计算了特征图，接着对特征图做简单的双线性插值运算，恢复到了原

图的大小。此方法提供了在密集预测任务中使用反卷积 [13], [14] 的一种简单而强大替代方法。与具有较大滤波器的常规卷积相比，空洞卷积允许我们有效地扩大滤波器的感受野而不增加参数的数量或计算量。

第二个挑战是由存在多个尺度的物体引起的。处理这一问题的标准做法是向 DCNNs 输入同一图像的不同缩放版本，然后聚合特征图或分数图 [6], [17], [18]。我们验证了这种方法的确能提升精度，但是对应一张图片要以其所有缩放版本的计算量为代价。然而，在空间金字塔池化方法 [19], [20] 的帮助下，我们使用了一种高效的计算方案，在进行卷积之前，以多种采样率重新采样给定的特征图。这相当于使用多个具有互补感受野的滤波器去处理原始图像，从而捕获物体及多个尺度下的图像上下文。我们使用多个并行的、具有不同采样率的空洞卷积，而不是真正地重新采样特征。这种组合技术我们称之为“空洞空间金字塔池化”（ASPP）。

第三个挑战涉及到这样一个事实，即以物体为中心的分类器需要空间变换不变性，从而固有地限制了 DCNNs 的空间精度。减轻精度下降的一种方法是，在计算最终分割结果时使用跳跃层从多个网络结构中抽取“超列” [14], [21]。我们研究探索了一种非常有效的替代办法——通过采用完全连接的条件随机场来提高模型捕获精细细节的能力 [22]。CRF 已广泛用于语义分割，以将由多路分类器计算的类分数与由像素和边缘 [23], [24] 或超像素 [25] 的局部低级信息组合。尽管已经提出了增加复杂性的工作来模拟分割依赖性 [26], [27], [28] 和（或）分段的高阶依赖性 [29], [30], [31], [32], [33]，但我们使用完全连接的成对 CRF 进行高效计算 [22]，并且在捕获精细边缘细节同时也适应了长时间的范围依赖。在 [22] 中提出的模型提升了像素级分类器的性能。在这项工作中，我们证明当与基于 DCNNs 的像素级分类器结合使用时，它能产生出色的结果。

Fig. 1 展示了我们提出的 DeepLab 模型的高层结构。在图像分类任务中训练的深度卷积网络（VGG-16 [4] 或 ResNet-101 [11]）通过以下方式重新运用于图像语义分割任务：(1) 将所有全连接层换成卷积层 [14]，(2) 通过空洞卷积层增加

• L.-C. Chen, G. Papandreou, and K. Murphy are with Google Inc. I. Kokkinos is with University College London. A. Yuille is with the Departments of Cognitive Science and Computer Science, Johns Hopkins University. The first two authors contributed equally to this work.

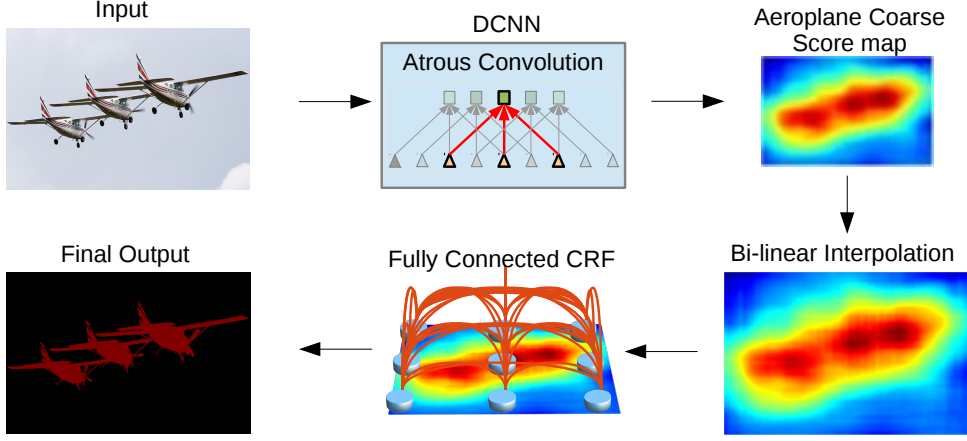


Fig. 1: 模型图。诸如 VGG-16 或 ResNet-101 之类的 DCNNs 以完全卷积的方式使用，使用空洞卷积来降低信号下采样的程度（从 $32\times$ 下降到 $8\times$ ）。双线性插值将特征放大到原始图像分辨率。然后使用完全连接的 CRF 来细化分割结并更好地捕获物体边界。

特征分辨率，使得我们能计算原图中每 8 个像素的特征而不是每 32 个。然后，我们采用双线性插值将分类分数图上采样 8 倍，以达到原图分辨率，从而产生全连接 CRF 的输入 [22]，来达到细化分割结果的目的。

从实用的角度来看，我们的 DeepLab 系统有三大优点：(1) 速度：由于空洞卷积的使用，我们的 DCNN 以 8 FPS 的速度在 NVidia Titan X GPU 上运行，全连接 CRF 的平均场推断在 CPU 上需要大约 0.5 秒；(2) 精度：在众多图像分割数据集挑战中，我们的模型一举夺魁，包括 PASCAL VOC 2012 [34], PASCAL-Context [35], PASCAL-Person-Part [36] 以及 Cityscapes [37]；(3) 复杂度：我们的系统是由 DCNNs 和 CRFs 这两个非常成熟的模块级联组合而成的，便于理解和编写。

这篇论文中介绍的更新过的 DeepLab 与我们最初发表的第一个版本相比有几项改进 [38]。新版本能够通过多尺度输入 [17], [39], [40] 或 ASPP 更好地分割多个尺度下的物体。我们通过调整最新的 ResNet [11] 图像分类 DCNN 构建了 DeepLab 的残差网络变体，与基于 VGG-16 [4] 的原始模型相比，拥有更优的语义分割性能。最后，我们对多种模型变体进行了更全面的实验评估，并报告了最新结果，不仅是 PASCAL VOC 2012，还有其他具有挑战性的任务。我们通过扩展 Caffe 框架 [41] 实现了 DeepLab，并在 <http://liangchihchen.com/projects/DeepLab.html> 开放了源代码及模型数据。

2 Related Work

Most of the successful semantic segmentation systems developed in the previous decade relied on hand-crafted features combined with flat classifiers, such as Boosting [24], [42], Random Forests [43], or Support Vector Machines [44]. Substantial improvements have been achieved by incorporating richer information from context [45] and structured prediction techniques [22], [26], [27], [46], but the performance of these systems has always been compromised by the limited expressive power of the features. Over the past few years the breakthroughs of Deep Learning in image classification were quickly transferred to the semantic segmentation task. Since this task involves both segmentation and classification, a central question is how to combine the two tasks.

The first family of DCNN-based systems for semantic segmentation typically employs a cascade of bottom-up image

segmentation, followed by DCNN-based region classification. For instance the bounding box proposals and masked regions delivered by [47], [48] are used in [7] and [49] as inputs to a DCNN to incorporate shape information into the classification process. Similarly, the authors of [50] rely on a superpixel representation. Even though these approaches can benefit from the sharp boundaries delivered by a good segmentation, they also cannot recover from any of its errors.

The second family of works relies on using convolutionally computed DCNN features for dense image labeling, and couples them with segmentations that are obtained independently. Among the first have been [39] who apply DCNNs at multiple image resolutions and then employ a segmentation tree to smooth the prediction results. More recently, [21] propose to use skip layers and concatenate the computed intermediate feature maps within the DCNNs for pixel classification. Further, [51] propose to pool the intermediate feature maps by region proposals. These works still employ segmentation algorithms that are decoupled from the DCNN classifier's results, thus risking commitment to premature decisions.

The third family of works uses DCNNs to directly provide dense category-level pixel labels, which makes it possible to even discard segmentation altogether. The segmentation-free approaches of [14], [52] directly apply DCNNs to the whole image in a fully convolutional fashion, transforming the last fully connected layers of the DCNN into convolutional layers. In order to deal with the spatial localization issues outlined in the introduction, [14] upsample and concatenate the scores from intermediate feature maps, while [52] refine the prediction result from coarse to fine by propagating the coarse results to another DCNN. Our work builds on these works, and as described in the introduction extends them by exerting control on the feature resolution, introducing multi-scale pooling techniques and integrating the densely connected CRF of [22] on top of the DCNN. We show that this leads to significantly better segmentation results, especially along object boundaries. The combination of DCNN and CRF is of course not new but previous works only tried locally connected CRF models. Specifically, [53] use CRFs as a proposal mechanism for a DCNN-based reranking system, while [39] treat superpixels as nodes for a local pairwise CRF

and use graph-cuts for discrete inference. As such their models were limited by errors in superpixel computations or ignored long-range dependencies. Our approach instead treats every pixel as a CRF node receiving unary potentials by the DCNN. Crucially, the Gaussian CRF potentials in the fully connected CRF model of [22] that we adopt can capture long-range dependencies and at the same time the model is amenable to fast mean field inference. We note that mean field inference had been extensively studied for traditional image segmentation tasks [54], [55], [56], but these older models were typically limited to short-range connections. In independent work, [57] use a very similar densely connected CRF model to refine the results of DCNN for the problem of material classification. However, the DCNN module of [57] was only trained by sparse point supervision instead of dense supervision at every pixel.

Since the first version of this work was made publicly available [38], the area of semantic segmentation has progressed drastically. Multiple groups have made important advances, significantly raising the bar on the PASCAL VOC 2012 semantic segmentation benchmark, as reflected to the high level of activity in the benchmark’s leaderboard¹ [17], [40], [58], [59], [60], [61], [62], [63]. Interestingly, most top-performing methods have adopted one or both of the key ingredients of our DeepLab system: Atrous convolution for efficient dense feature extraction and refinement of the raw DCNN scores by means of a fully connected CRF. We outline below some of the most important and interesting advances.

End-to-end training for structured prediction has more recently been explored in several related works. While we employ the CRF as a post-processing method, [40], [59], [62], [64], [65] have successfully pursued joint learning of the DCNN and CRF. In particular, [59], [65] unroll the CRF mean-field inference steps to convert the whole system into an end-to-end trainable feed-forward network, while [62] approximates one iteration of the dense CRF mean field inference [22] by convolutional layers with learnable filters. Another fruitful direction pursued by [40], [66] is to learn the pairwise terms of a CRF via a DCNN, significantly improving performance at the cost of heavier computation. In a different direction, [63] replace the bilateral filtering module used in mean field inference with a faster domain transform module [67], improving the speed and lowering the memory requirements of the overall system, while [18], [68] combine semantic segmentation with edge detection.

Weaker supervision has been pursued in a number of papers, relaxing the assumption that pixel-level semantic annotations are available for the whole training set [58], [69], [70], [71], achieving significantly better results than weakly-supervised pre-DCNN systems such as [72]. In another line of research, [49], [73] pursue instance segmentation, jointly tackling object detection and semantic segmentation.

What we call here *atrous convolution* was originally developed for the efficient computation of the undecimated wavelet transform in the “algorithme à trous” scheme of [15]. We refer the interested reader to [74] for early references from the wavelet literature. Atrous convolution is also intimately related to the “noble identities” in multi-rate signal processing, which builds on the same interplay of input signal and filter sampling rates [75]. Atrous convolution is a term we

first used in [6]. The same operation was later called dilated convolution by [76], a term they coined motivated by the fact that the operation corresponds to regular convolution with upsampled (or dilated in the terminology of [15]) filters. Various authors have used the same operation before for denser feature extraction in DCNNs [3], [6], [16]. Beyond mere resolution enhancement, atrous convolution allows us to enlarge the field of view of filters to incorporate larger context, which we have shown in [38] to be beneficial. This approach has been pursued further by [76], who employ a series of atrous convolutional layers with increasing rates to aggregate multiscale context. The atrous spatial pyramid pooling scheme proposed here to capture multiscale objects and context also employs multiple atrous convolutional layers with different sampling rates, which we however lay out in parallel instead of in serial. Interestingly, the atrous convolution technique has also been adopted for a broader set of tasks, such as object detection [12], [77], instance-level segmentation [78], visual question answering [79], and optical flow [80].

We also show that, as expected, integrating into DeepLab more advanced image classification DCNNs such as the residual net of [11] leads to better results. This has also been observed independently by [81].

3 Methods

3.1 Atrous Convolution for Dense Feature Extraction and Field-of-View Enlargement

The use of DCNNs for semantic segmentation, or other dense prediction tasks, has been shown to be simply and successfully addressed by deploying DCNNs in a fully convolutional fashion [3], [14]. However, the repeated combination of max-pooling and striding at consecutive layers of these networks reduces significantly the spatial resolution of the resulting feature maps, typically by a factor of 32 across each direction in recent DCNNs. A partial remedy is to use ‘deconvolutional’ layers as in [14], which however requires additional memory and time.

We advocate instead the use of atrous convolution, originally developed for the efficient computation of the undecimated wavelet transform in the “algorithme à trous” scheme of [15] and used before in the DCNN context by [3], [6], [16]. This algorithm allows us to compute the responses of any layer at any desirable resolution. It can be applied post-hoc, once a network has been trained, but can also be seamlessly integrated with training.

Considering one-dimensional signals first, the output $y[i]$ of atrous convolution² of a 1-D input signal $x[i]$ with a filter $w[k]$ of length K is defined as:

$$y[i] = \sum_{k=1}^K x[i + r \cdot k]w[k]. \quad (1)$$

The *rate* parameter r corresponds to the stride with which we sample the input signal. Standard convolution is a special case for rate $r = 1$. See Fig. 2 for illustration.

We illustrate the algorithm’s operation in 2-D through a simple example in Fig. 3: Given an image, we assume that we

1. <http://host.robots.ox.ac.uk:8080/leaderboard/displaylb.php?challengeid=11&compid=6>

2. We follow the standard practice in the DCNN literature and use non-mirrored filters in this definition.

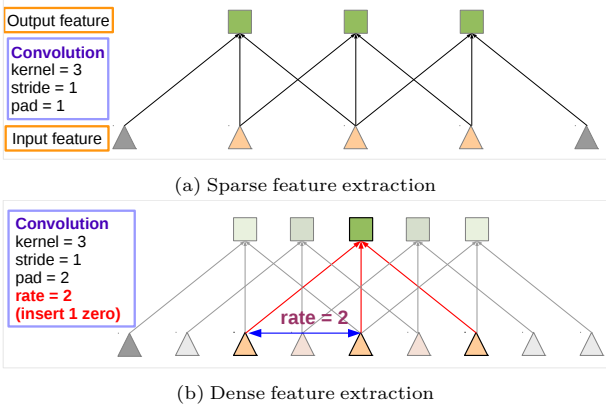


Fig. 2: Illustration of atrous convolution in 1-D. (a) Sparse feature extraction with standard convolution on a low resolution input feature map. (b) Dense feature extraction with atrous convolution with rate $r = 2$, applied on a high resolution input feature map.

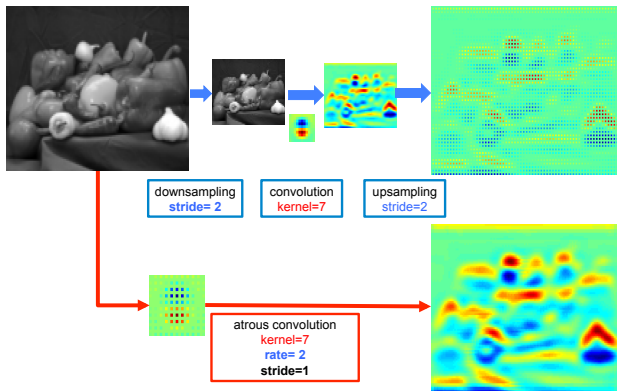


Fig. 3: Illustration of atrous convolution in 2-D. Top row: sparse feature extraction with standard convolution on a low resolution input feature map. Bottom row: Dense feature extraction with atrous convolution with rate $r = 2$, applied on a high resolution input feature map.

first have a downsampling operation that reduces the resolution by a factor of 2, and then perform a convolution with a kernel - here, the vertical Gaussian derivative. If one implants the resulting feature map in the original image coordinates, we realize that we have obtained responses at only 1/4 of the image positions. Instead, we can compute responses at all image positions if we convolve the full resolution image with a filter ‘with holes’, in which we upsample the original filter by a factor of 2, and introduce zeros in between filter values. Although the effective filter size increases, we only need to take into account the non-zero filter values, hence both the number of filter parameters and the number of operations per position stay constant. The resulting scheme allows us to easily and explicitly control the spatial resolution of neural network feature responses.

In the context of DCNNs one can use atrous convolution in a chain of layers, effectively allowing us to compute the final DCNN network responses at an arbitrarily high resolution. For example, in order to double the spatial density

of computed feature responses in the VGG-16 or ResNet-101 networks, we find the last pooling or convolutional layer that decreases resolution (‘pool5’ or ‘conv5_1’ respectively), set its stride to 1 to avoid signal decimation, and replace all subsequent convolutional layers with atrous convolutional layers having rate $r = 2$. Pushing this approach all the way through the network could allow us to compute feature responses at the original image resolution, but this ends up being too costly. We have adopted instead a hybrid approach that strikes a good efficiency/accuracy trade-off, using atrous convolution to increase by a factor of 4 the density of computed feature maps, followed by fast bilinear interpolation by an additional factor of 8 to recover feature maps at the original image resolution. Bilinear interpolation is sufficient in this setting because the class score maps (corresponding to log-probabilities) are quite smooth, as illustrated in Fig. 5. Unlike the deconvolutional approach adopted by [14], the proposed approach converts image classification networks into dense feature extractors without requiring learning any extra parameters, leading to faster DCNN training in practice.

Atrous convolution also allows us to arbitrarily enlarge the *field-of-view* of filters at any DCNN layer. State-of-the-art DCNNs typically employ spatially small convolution kernels (typically 3×3) in order to keep both computation and number of parameters contained. Atrous convolution with rate r introduces $r - 1$ zeros between consecutive filter values, effectively enlarging the kernel size of a $k \times k$ filter to $k_e = k + (k-1)(r-1)$ without increasing the number of parameters or the amount of computation. It thus offers an efficient mechanism to control the field-of-view and finds the best trade-off between accurate localization (small field-of-view) and context assimilation (large field-of-view). We have successfully experimented with this technique: Our DeepLab-LargeFOV model variant [38] employs atrous convolution with rate $r = 12$ in VGG-16 ‘fc6’ layer with significant performance gains, as detailed in Section 4.

Turning to implementation aspects, there are two efficient ways to perform atrous convolution. The first is to implicitly upsample the filters by inserting holes (zeros), or equivalently sparsely sample the input feature maps [15]. We implemented this in our earlier work [6], [38], followed by [76], within the Caffe framework [41] by adding to the *im2col* function (it extracts vectorized patches from multi-channel feature maps) the option to sparsely sample the underlying feature maps. The second method, originally proposed by [82] and used in [3], [16] is to subsample the input feature map by a factor equal to the atrous convolution rate r , deinterlacing it to produce r^2 reduced resolution maps, one for each of the $r \times r$ possible shifts. This is followed by applying standard convolution to these intermediate feature maps and reinterlacing them to the original image resolution. By reducing atrous convolution into regular convolution, it allows us to use off-the-shelf highly optimized convolution routines. We have implemented the second approach into the TensorFlow framework [83].

3.2 Multiscale Image Representations using Atrous Spatial Pyramid Pooling

DCNNs have shown a remarkable ability to implicitly represent scale, simply by being trained on datasets that contain objects of varying size. Still, explicitly accounting for object

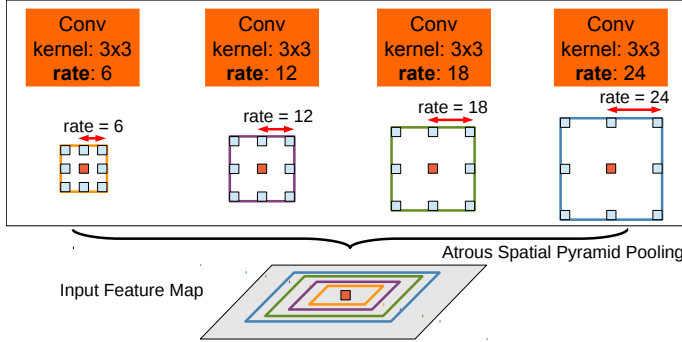


Fig. 4: Atrous Spatial Pyramid Pooling (ASPP). To classify the center pixel (orange), ASPP exploits multi-scale features by employing multiple parallel filters with different rates. The effective Field-Of-Views are shown in different colors.

scale can improve the DCNN’s ability to successfully handle both large and small objects [6].

We have experimented with two approaches to handling scale variability in semantic segmentation. The first approach amounts to standard multiscale processing [17], [18]. We extract DCNN score maps from multiple (three in our experiments) rescaled versions of the original image using parallel DCNN branches that share the same parameters. To produce the final result, we bilinearly interpolate the feature maps from the parallel DCNN branches to the original image resolution and fuse them, by taking at each position the maximum response across the different scales. We do this both during training and testing. Multiscale processing significantly improves performance, but at the cost of computing feature responses at all DCNN layers for multiple scales of input.

The second approach is inspired by the success of the R-CNN spatial pyramid pooling method of [20], which showed that regions of an arbitrary scale can be accurately and efficiently classified by resampling convolutional features extracted at a single scale. We have implemented a variant of their scheme which uses multiple parallel atrous convolutional layers with different sampling rates. The features extracted for each sampling rate are further processed in separate branches and fused to generate the final result. The proposed “atrous spatial pyramid pooling” (DeepLab-ASPP) approach generalizes our DeepLab-LargeFOV variant and is illustrated in Fig. 4.

3.3 Structured Prediction with Fully-Connected Conditional Random Fields for Accurate Boundary Recovery

A trade-off between localization accuracy and classification performance seems to be inherent in DCNNs: deeper models with multiple max-pooling layers have proven most successful in classification tasks, however the increased invariance and the large receptive fields of top-level nodes can only yield smooth responses. As illustrated in Fig. 5, DCNN score maps can predict the presence and rough position of objects but cannot really delineate their borders.

Previous work has pursued two directions to address this localization challenge. The first approach is to harness information from multiple layers in the convolutional network in order to better estimate the object boundaries [14], [21],

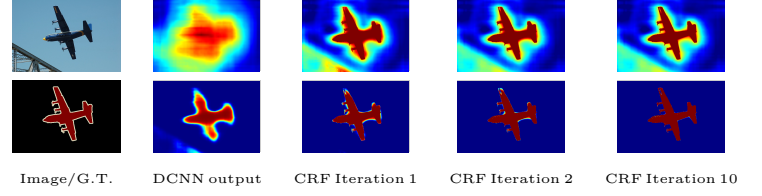


Fig. 5: Score map (input before softmax function) and belief map (output of softmax function) for Aeroplane. We show the score (1st row) and belief (2nd row) maps after each mean field iteration. The output of last DCNN layer is used as input to the mean field inference.

[52]. The second is to employ a super-pixel representation, essentially delegating the localization task to a low-level segmentation method [50].

We pursue an alternative direction based on coupling the recognition capacity of DCNNs and the fine-grained localization accuracy of fully connected CRFs and show that it is remarkably successful in addressing the localization challenge, producing accurate semantic segmentation results and recovering object boundaries at a level of detail that is well beyond the reach of existing methods. This direction has been extended by several follow-up papers [17], [40], [58], [59], [60], [61], [62], [63], [65], since the first version of our work was published [38].

Traditionally, conditional random fields (CRFs) have been employed to smooth noisy segmentation maps [23], [31]. Typically these models couple neighboring nodes, favoring same-label assignments to spatially proximal pixels. Qualitatively, the primary function of these short-range CRFs is to clean up the spurious predictions of weak classifiers built on top of local hand-engineered features.

Compared to these weaker classifiers, modern DCNN architectures such as the one we use in this work produce score maps and semantic label predictions which are qualitatively different. As illustrated in Fig. 5, the score maps are typically quite smooth and produce homogeneous classification results. In this regime, using short-range CRFs can be detrimental, as our goal should be to recover detailed local structure rather than further smooth it. Using contrast-sensitive potentials [23] in conjunction to local-range CRFs can potentially improve localization but still miss thin-structures and typically requires solving an expensive discrete optimization problem.

To overcome these limitations of short-range CRFs, we integrate into our system the fully connected CRF model of [22]. The model employs the energy function

$$E(\mathbf{x}) = \sum_i \theta_i(x_i) + \sum_{ij} \theta_{ij}(x_i, x_j) \quad (2)$$

where \mathbf{x} is the label assignment for pixels. We use as unary potential $\theta_i(x_i) = -\log P(x_i)$, where $P(x_i)$ is the label assignment probability at pixel i as computed by a DCNN. The pairwise potential has a form that allows for efficient inference while using a fully-connected graph, i.e. when connecting all pairs of image pixels, i, j . In particular, as in [22], we use the

following expression:

$$\theta_{ij}(x_i, x_j) = \mu(x_i, x_j) \left[w_1 \exp \left(-\frac{\|p_i - p_j\|^2}{2\sigma_\alpha^2} - \frac{\|I_i - I_j\|^2}{2\sigma_\beta^2} \right) + w_2 \exp \left(-\frac{\|p_i - p_j\|^2}{2\sigma_\gamma^2} \right) \right] \quad (3)$$

where $\mu(x_i, x_j) = 1$ if $x_i \neq x_j$, and zero otherwise, which, as in the Potts model, means that only nodes with distinct labels are penalized. The remaining expression uses two Gaussian kernels in different feature spaces; the first, ‘bilateral’ kernel depends on both pixel positions (denoted as p) and RGB color (denoted as I), and the second kernel only depends on pixel positions. The hyper parameters σ_α , σ_β and σ_γ control the scale of Gaussian kernels. The first kernel forces pixels with similar color and position to have similar labels, while the second kernel only considers spatial proximity when enforcing smoothness.

Crucially, this model is amenable to efficient approximate probabilistic inference [22]. The message passing updates under a fully decomposable mean field approximation $b(\mathbf{x}) = \prod_i b_i(x_i)$ can be expressed as Gaussian convolutions in bilateral space. High-dimensional filtering algorithms [84] significantly speed-up this computation resulting in an algorithm that is very fast in practice, requiring less than 0.5 sec on average for Pascal VOC images using the publicly available implementation of [22].

4 Experimental Results

We finetune the model weights of the Imagenet-pretrained VGG-16 or ResNet-101 networks to adapt them to the semantic segmentation task in a straightforward fashion, following the procedure of [14]. We replace the 1000-way Imagenet classifier in the last layer with a classifier having as many targets as the number of semantic classes of our task (including the background, if applicable). Our loss function is the sum of cross-entropy terms for each spatial position in the CNN output map (subsampled by 8 compared to the original image). All positions and labels are equally weighted in the overall loss function (except for unlabeled pixels which are ignored). Our targets are the ground truth labels (subsampled by 8). We optimize the objective function with respect to the weights at all network layers by the standard SGD procedure of [2]. We decouple the DCNN and CRF training stages, assuming the DCNN unary terms are fixed when setting the CRF parameters.

We evaluate the proposed models on four challenging datasets: PASCAL VOC 2012, PASCAL-Context, PASCAL-Person-Part, and Cityscapes. We first report the main results of our conference version [38] on PASCAL VOC 2012, and move forward to latest results on all datasets.

4.1 PASCAL VOC 2012

Dataset: The PASCAL VOC 2012 segmentation benchmark [34] involves 20 foreground object classes and one background class. The original dataset contains 1,464 (*train*), 1,449 (*val*), and 1,456 (*test*) pixel-level labeled images for training, validation, and testing, respectively. The dataset is augmented by the extra annotations provided by [85], resulting in 10,582 (*trainaug*) training images. The performance is measured in

Kernel	Rate	FOV	Params	Speed	bef/aft CRF
7×7	4	224	134.3M	1.44	64.38 / 67.64
4×4	4	128	65.1M	2.90	59.80 / 63.74
4×4	8	224	65.1M	2.90	63.41 / 67.14
3×3	12	224	20.5M	4.84	62.25 / 67.64

TABLE 1: Effect of Field-Of-View by adjusting the kernel size and atrous sampling rate r at ‘fc6’ layer. We show number of model parameters, training speed (img/sec), and *val* set mean IOU before and after CRF. DeepLab-LargeFOV (kernel size 3×3 , $r = 12$) strikes the best balance.

terms of pixel intersection-over-union (IOU) averaged across the 21 classes.

4.1.1 Results from our conference version

We employ the VGG-16 network pre-trained on Imagenet, adapted for semantic segmentation as described in Section 3.1. We use a mini-batch of 20 images and initial learning rate of 0.001 (0.01 for the final classifier layer), multiplying the learning rate by 0.1 every 2000 iterations. We use momentum of 0.9 and weight decay of 0.0005.

After the DCNN has been fine-tuned on *trainaug*, we cross-validate the CRF parameters along the lines of [22]. We use default values of $w_2 = 3$ and $\sigma_\gamma = 3$ and we search for the best values of w_1 , σ_α , and σ_β by cross-validation on 100 images from *val*. We employ a coarse-to-fine search scheme. The initial search range of the parameters are $w_1 \in [3 : 6]$, $\sigma_\alpha \in [30 : 10 : 100]$ and $\sigma_\beta \in [3 : 6]$ (MATLAB notation), and then we refine the search step sizes around the first round’s best values. We employ 10 mean field iterations.

Field of View and CRF: In Tab. 1, we report experiments with DeepLab model variants that use different field-of-view sizes, obtained by adjusting the kernel size and atrous sampling rate r in the ‘fc6’ layer, as described in Sec. 3.1. We start with a direct adaptation of VGG-16 net, using the original 7×7 kernel size and $r = 4$ (since we use no stride for the last two max-pooling layers). This model yields performance of 67.64% after CRF, but is relatively slow (1.44 images per second during training). We have improved model speed to 2.9 images per second by reducing the kernel size to 4×4 . We have experimented with two such network variants with smaller ($r = 4$) and larger ($r = 8$) FOV sizes; the latter one performs better. Finally, we employ kernel size 3×3 and even larger atrous sampling rate ($r = 12$), also making the network thinner by retaining a random subset of 1,024 out of the 4,096 filters in layers ‘fc6’ and ‘fc7’. The resulting model, DeepLab-CRF-LargeFOV, matches the performance of the direct VGG-16 adaptation (7×7 kernel size, $r = 4$). At the same time, DeepLab-LargeFOV is 3.36 times faster and has significantly fewer parameters (20.5M instead of 134.3M).

The CRF substantially boosts performance of all model variants, offering a 3–5% absolute increase in mean IOU.

Test set evaluation: We have evaluated our DeepLab-CRF-LargeFOV model on the PASCAL VOC 2012 official *test* set. It achieves 70.3% mean IOU performance.

4.1.2 Improvements after conference version of this work

After the conference version of this work [38], we have pursued three main improvements of our model, which we discuss below: (1) different learning policy during training, (2) atrous

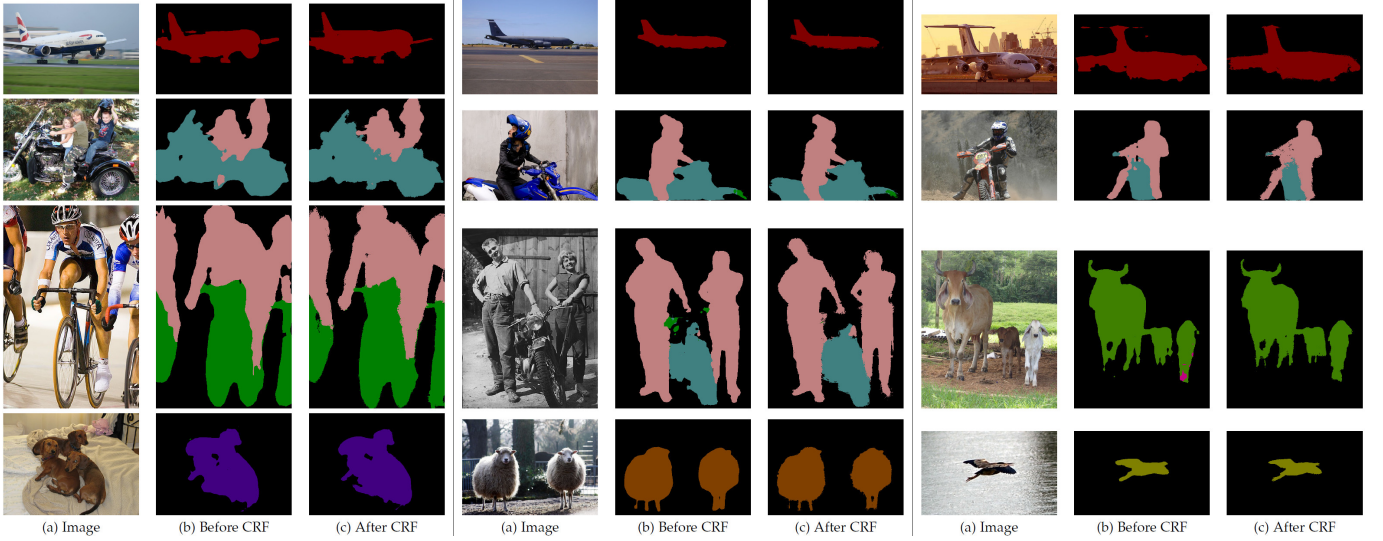


Fig. 6: PASCAL VOC 2012 *val* results. Input image and our DeepLab results before/after CRF.

Learning policy	Batch size	Iteration	mean IOU
step	30	6K	62.25
poly	30	6K	63.42
poly	30	10K	64.90
poly	10	10K	64.71
poly	10	20K	65.88

TABLE 2: PASCAL VOC 2012 *val* set results (%) (before CRF) as different learning hyper parameters vary. Employing “poly” learning policy is more effective than “step” when training DeepLab-LargeFOV.

spatial pyramid pooling, and (3) employment of deeper networks and multi-scale processing.

Learning rate policy: We have explored different learning rate policies when training DeepLab-LargeFOV. Similar to [86], we also found that employing a “poly” learning rate policy (the learning rate is multiplied by $(1 - \frac{\text{iter}}{\text{max_iter}})^{\text{power}}$) is more effective than “step” learning rate (reduce the learning rate at a fixed step size). As shown in Tab. 2, employing “poly” (with $\text{power} = 0.9$) and using the same batch size and same training iterations yields 1.17% better performance than employing “step” policy. Fixing the batch size and increasing the training iteration to 10K improves the performance to 64.90% (1.48% gain); however, the total training time increases due to more training iterations. We then reduce the batch size to 10 and found that comparable performance is still maintained (64.90% vs. 64.71%). In the end, we employ batch size = 10 and 20K iterations in order to maintain similar training time as previous “step” policy. Surprisingly, this gives us the performance of 65.88% (3.63% improvement over “step”) on *val*, and 67.7% on *test*, compared to 65.1% of the original “step” setting for DeepLab-LargeFOV before CRF. We employ the “poly” learning rate policy for all experiments reported in the rest of the paper.

Atrous Spatial Pyramid Pooling: We have experimented with the proposed Atrous Spatial Pyramid Pooling (ASPP) scheme, described in Sec. 3.1. As shown in Fig. 7, ASPP for VGG-16 employs several parallel fc6-fc7-

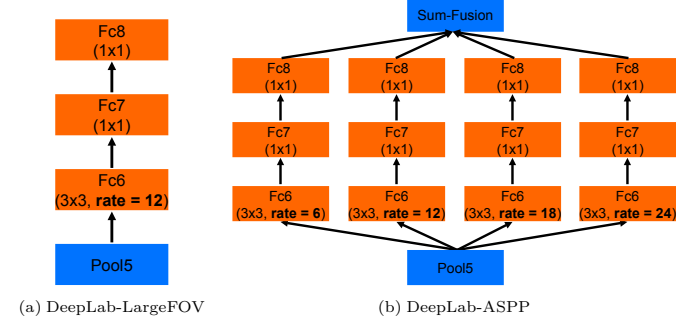


Fig. 7: DeepLab-ASPP employs multiple filters with different rates to capture objects and context at multiple scales.

fc8 branches. They all use 3×3 kernels but different atrous rates r in the ‘fc6’ in order to capture objects of different size. In Tab. 3, we report results with several settings: (1) Our baseline LargeFOV model, having a single branch with $r = 12$, (2) ASPP-S, with four branches and smaller atrous rates ($r = \{2, 4, 8, 12\}$), and (3) ASPP-L, with four branches and larger rates ($r = \{6, 12, 18, 24\}$). For each variant we report results before and after CRF. As shown in the table, ASPP-S yields 1.22% improvement over the baseline LargeFOV before CRF. However, after CRF both LargeFOV and ASPP-S perform similarly. On the other hand, ASPP-L yields consistent improvements over the baseline LargeFOV both before and after CRF. We evaluate on *test* the proposed ASPP-L + CRF model, attaining 72.6%. We visualize the effect of the different schemes in Fig. 8.

Deeper Networks and Multiscale Processing: We have experimented building DeepLab around the recently proposed residual net ResNet-101 [11] instead of VGG-16. Similar to what we did for VGG-16 net, we re-purpose ResNet-101 by atrous convolution, as described in Sec. 3.1. On top of that, we adopt several other features, following recent work of [17], [18], [39], [40], [58], [59], [62]: (1) Multi-scale inputs: We separately feed to the DCNN images at scale = $\{0.5, 0.75, 1\}$, fusing their score maps by taking the maximum

Method	before CRF	after CRF
LargeFOV	65.76	69.84
ASPP-S	66.98	69.73
ASPP-L	68.96	71.57

TABLE 3: Effect of ASPP on PASCAL VOC 2012 *val* set performance (mean IOU) for VGG-16 based DeepLab model. **LargeFOV**: single branch, $r = 12$. **ASPP-S**: four branches, $r = \{2, 4, 8, 12\}$. **ASPP-L**: four branches, $r = \{6, 12, 18, 24\}$.

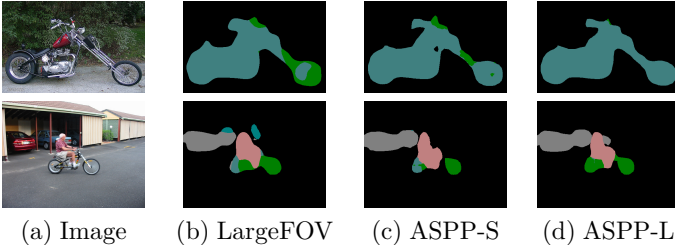


Fig. 8: Qualitative segmentation results with ASPP compared to the baseline LargeFOV model. The **ASPP-L** model, employing multiple *large* FOVs can successfully capture objects as well as image context at multiple scales.

MSC	COCO	Aug	LargeFOV	ASPP	CRF	mIOU
✓						68.72
✓		✓				71.27
✓	✓		✓			73.28
✓	✓	✓	✓	✓		74.87
✓	✓	✓	✓		✓	75.54
✓	✓	✓		✓		76.35
✓	✓	✓		✓	✓	77.69

TABLE 4: Employing ResNet-101 for DeepLab on PASCAL VOC 2012 *val* set. **MSC**: Employing mutli-scale inputs with max fusion. **COCO**: Models pretrained on MS-COCO. **Aug**: Data augmentation by randomly rescaling inputs.

response across scales for each position separately [17]. (2) Models pretrained on MS-COCO [87]. (3) Data augmentation by randomly scaling the input images (from 0.5 to 1.5) during training. In Tab. 4, we evaluate how each of these factors, along with LargeFOV and atrous spatial pyramid pooling (ASPP), affects *val* set performance. Adopting ResNet-101 instead of VGG-16 significantly improves DeepLab performance (*e.g.*, our simplest ResNet-101 based model attains 68.72%, compared to 65.76% of our DeepLab-LargeFOV VGG-16 based variant, both before CRF). Multiscale fusion [17] brings extra 2.55% improvement, while pretraining the model on MS-COCO gives another 2.01% gain. Data augmentation during training is effective (about 1.6% improvement). Employing LargeFOV (adding an atrous convolutional layer on top of ResNet, with 3×3 kernel and rate = 12) is beneficial (about 0.6% improvement). Further 0.8% improvement is achieved by atrous spatial pyramid pooling (ASPP). Post-processing our best model by dense CRF yields performance of 77.69%.

Qualitative results: We provide qualitative visual comparisons of DeepLab’s results (our best model variant) before and after CRF in Fig. 6. The visualization results obtained by DeepLab before CRF already yields excellent segmentation results, while employing the CRF further improves the

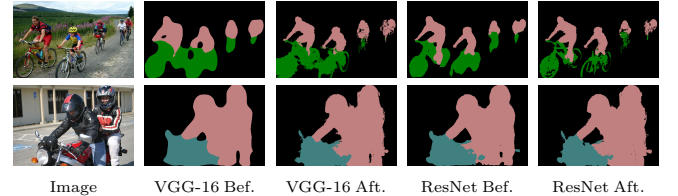


Fig. 9: DeepLab results based on VGG-16 net or ResNet-101 before and after CRF. The CRF is critical for accurate prediction along object boundaries with VGG-16, whereas ResNet-101 has acceptable performance even before CRF.

performance by removing false positives and refining object boundaries.

Test set results: We have submitted the result of our final best model to the official server, obtaining *test* set performance of 79.7%, as shown in Tab. 5. The model substantially outperforms previous DeepLab variants (*e.g.*, DeepLab-LargeFOV with VGG-16 net) and is currently the top performing method on the PASCAL VOC 2012 segmentation leaderboard.

Method	mIOU
DeepLab-CRF-LargeFOV-COCO [58]	72.7
MERL_DEEP_GCRF [88]	73.2
CRF-RNN [59]	74.7
POSTECH_DeconvNet_CRF_VOC [61]	74.8
BoxSup [60]	75.2
Context + CRF-RNN [76]	75.3
QO_4^{mres} [66]	75.5
DeepLab-CRF-Attention [17]	75.7
CentraleSuperBoundaries++ [18]	76.0
DeepLab-CRF-Attention-DT [63]	76.3
H-ReNet + DenseCRF [89]	76.8
LRR_4x_COCO [90]	76.8
DPN [62]	77.5
Adelaide_Context [40]	77.8
Oxford_TVGH_O_CRF [91]	77.9
Context CRF + Guidance CRF [92]	78.1
Adelaide_VeryDeep_FCN_VOC [93]	79.1
DeepLab-CRF (ResNet-101)	79.7

TABLE 5: Performance on PASCAL VOC 2012 *test* set. We have added some results from recent arXiv papers on top of the official leadearboard results.

VGG-16 vs. ResNet-101: We have observed that DeepLab based on ResNet-101 [11] delivers better segmentation results along object boundaries than employing VGG-16 [4], as visualized in Fig. 9. We think the identity mapping [94] of ResNet-101 has similar effect as hyper-column features [21], which exploits the features from the intermediate layers to better localize boundaries. We further quantize this effect in Fig. 10 within the “trimap” [22], [31] (a narrow band along object boundaries). As shown in the figure, employing ResNet-101 before CRF has almost the same accuracy along object boundaries as employing VGG-16 in conjunction with a CRF. Post-processing the ResNet-101 result with a CRF further improves the segmentation result.

4.2 PASCAL-Context

Dataset: The PASCAL-Context dataset [35] provides detailed semantic labels for the whole scene, including both

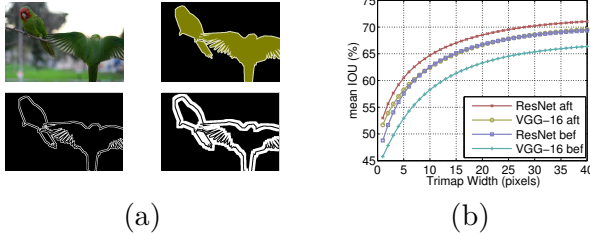


Fig. 10: (a) Trimap examples (top-left: image. top-right: ground-truth. bottom-left: trimap of 2 pixels. bottom-right: trimap of 10 pixels). (b) Pixel mean IOU as a function of the band width around the object boundaries when employing VGG-16 or ResNet-101 before and after CRF.

Method	MSC	COCO	Aug	LargeFOV	ASPP	CRF	mIOU
<i>VGG-16</i>							
DeepLab [38]			✓				37.6
DeepLab [38]			✓		✓		39.6
<i>ResNet-101</i>							
DeepLab							58.90
DeepLab	✓					✓	63.10
DeepLab	✓			✓	✓	✓	64.40
DeepLab	✓			✓	✓	✓	64.94
DeepLab	✓				✓	✓	62.18
DeepLab	✓				✓	✓	62.76
Attention [17]							56.39
HAZN [95]							57.54
LG-LSTM [96]							57.97
Graph LSTM [97]							60.16

TABLE 7: Comparison with other state-of-art methods on PASCAL-Person-Part dataset.

improve the prediction along object/stuff boundaries.	56.39
37.6	57.54
39.6	57.97

4.3 PASCAL-Person-Part

Dataset: We further perform experiments on semantic part segmentation [98], [99], using the extra PASCAL VOC 2010 annotations by [36]. We focus on the *person* part for the dataset, which contains more training data and large variation in object scale and human pose. Specifically, the dataset contains detailed part annotations for every person, e.g. eyes, nose. We merge the annotations to be Head, Torso, Upper/Lower Arms and Upper/Lower Legs, resulting in six person part classes and one background class. We only use those images containing persons for training (1716 images) and validation (1817 images).

Evaluation: The human part segmentation results on PASCAL-Person-Part is reported in Tab. 7. [17] has already conducted experiments on this dataset with re-purposed VGG-16 net for DeepLab, attaining 56.39% (with multi-scale inputs). Therefore, in this part, we mainly focus on the effect of repurposing ResNet-101 for DeepLab. With ResNet-101, DeepLab alone yields 58.9%, significantly outperforming DeepLab-LargeFOV (VGG-16 net) and DeepLab-Attention (VGG-16 net) by about 7% and 2.5%, respectively. Incorporating multi-scale inputs and fusion by max-pooling further improves performance to 63.1%. Additionally pretraining the model on MS-COCO yields another 1.3% improvement. However, we do not observe any improvement when adopting either LargeFOV or ASPP on this dataset. Employing the dense CRF to post process our final output substantially outperforms the concurrent work [97] by 4.78%.

Qualitative results: We visualize the results in Fig. 12.

4.4 Cityscapes

Dataset: Cityscapes [37] is a recently released large-scale dataset, which contains high quality pixel-level annotations of 5000 images collected in street scenes from 50 different cities. Following the evaluation protocol [37], 19 semantic labels (belonging to 7 super categories: ground, construction, object, nature, sky, human, and vehicle) are used for evaluation (the void label is not considered for evaluation). The training, validation, and test sets contain 2975, 500, and 1525 images respectively.

Test set results of pre-release: We have participated in benchmarking the Cityscapes dataset pre-release. As shown

TABLE 6: Comparison with other state-of-art methods on PASCAL-Context dataset.

object (*e.g.*, person) and stuff (*e.g.*, sky). Following [35], the proposed models are evaluated on the most frequent 59 classes along with one background category. The training set and validation set contain 4998 and 5105 images.

Evaluation: We report the evaluation results in Tab. 6. Our VGG-16 based LargeFOV variant yields 37.6% before and 39.6% after CRF. Repurposing the ResNet-101 [11] for DeepLab improves 2% over the VGG-16 LargeFOV. Similar to [17], employing multi-scale inputs and max-pooling to merge the results improves the performance to 41.4%. Pretraining the model on MS-COCO brings extra 1.5% improvement. Employing atrous spatial pyramid pooling is more effective than LargeFOV. After further employing dense CRF as post processing, our final model yields 45.7%, outperforming the current state-of-art method [40] by 2.4% without using their non-linear pairwise term. Our final model is slightly better than the concurrent work [93] by 1.2%, which also employs atrous convolution to repurpose the residual net of [11] for semantic segmentation.

Qualitative results: We visualize the segmentation results of our best model with and without CRF as post processing in Fig. 11. DeepLab before CRF can already predict most of the object/stuff with high accuracy. Employing CRF, our model is able to further remove isolated false positives and

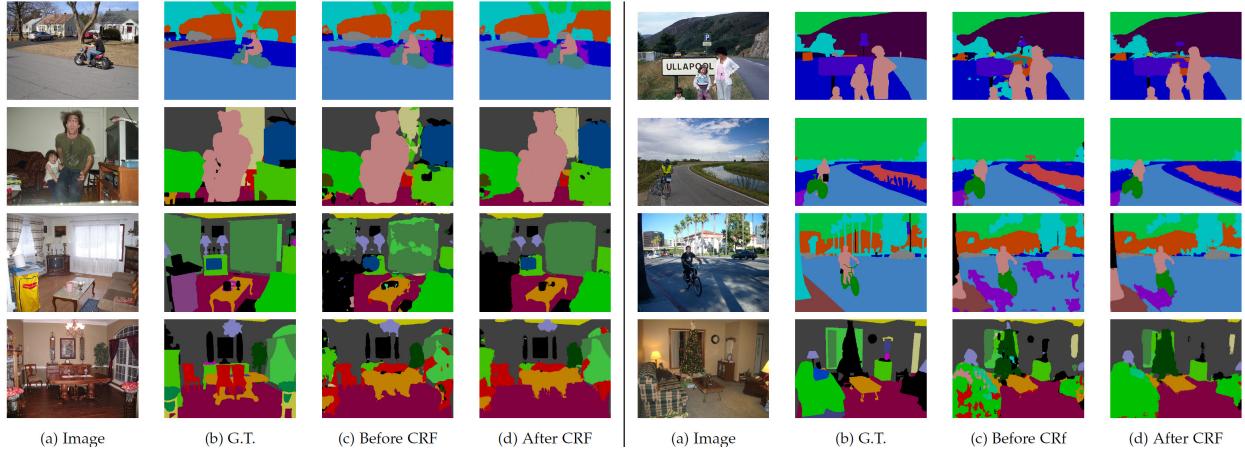


Fig. 11: PASCAL-Context results. Input image, ground-truth, and our DeepLab results before/after CRF.

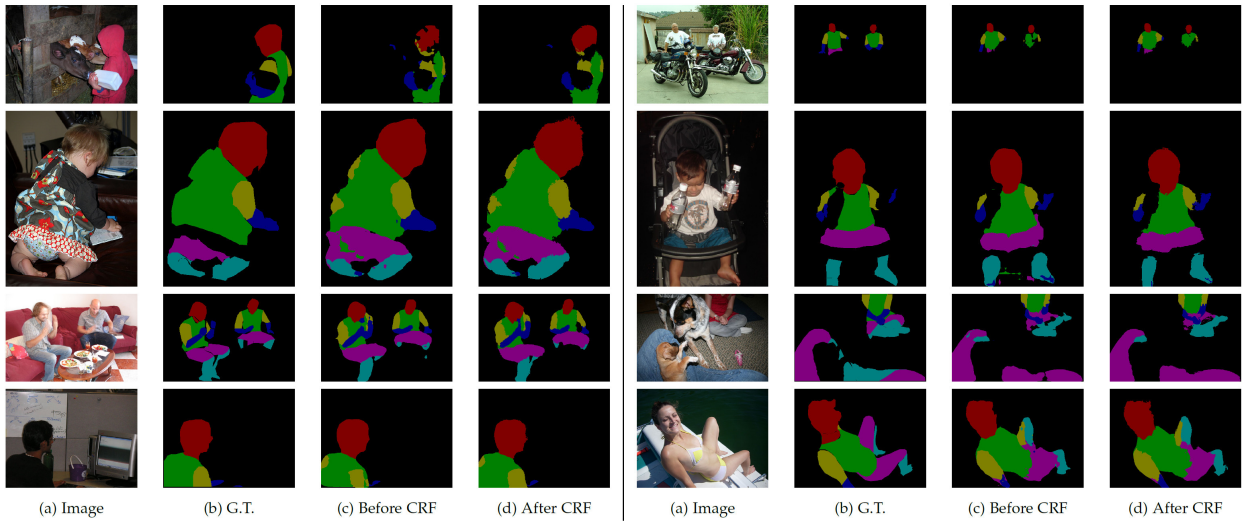


Fig. 12: PASCAL-Person-Part results. Input image, ground-truth, and our DeepLab results before/after CRF.

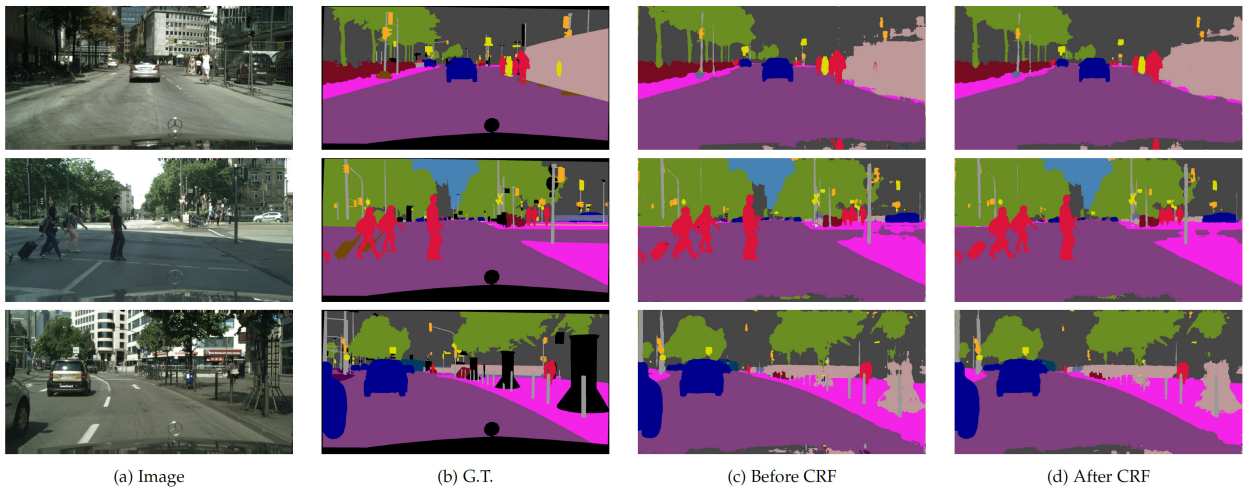


Fig. 13: Cityscapes results. Input image, ground-truth, and our DeepLab results before/after CRF.

in the top of Tab. 8, our model attained third place, with performance of 63.1% and 64.8% (with training on additional coarsely annotated images).

Val set results: After the initial release, we further explored the validation set in Tab. 9. The images of Cityscapes have resolution 2048×1024 , making it a challenging problem

Method	mIOU
<i>pre-release version of dataset</i>	
Adelaide_Context [40]	66.4
FCN-8s [14]	65.3
DeepLab-CRF-LargeFOV-StrongWeak [58]	64.8
DeepLab-CRF-LargeFOV [38]	63.1
CRF-RNN [59]	62.5
DPN [62]	59.1
Segnet basic [100]	57.0
Segnet extended [100]	56.1
<i>official version</i>	
Adelaide_Context [40]	71.6
Dilation10 [76]	67.1
DPN [62]	66.8
Pixel-level Encoding [101]	64.3
DeepLab-CRF (ResNet-101)	70.4

TABLE 8: Test set results on the Cityscapes dataset, comparing our DeepLab system with other state-of-art methods.

Full	Aug	LargeFOV	ASPP	CRF	mIOU
<i>VGG-16</i>					
		✓			62.97
		✓		✓	64.18
✓		✓			64.89
✓		✓		✓	65.94
<i>ResNet-101</i>					
✓					66.6
✓		✓			69.2
✓			✓		70.4
✓	✓		✓		71.0
✓	✓		✓	✓	71.4

TABLE 9: Val set results on Cityscapes dataset. **Full**: model trained with full resolution images.

to train deeper networks with limited GPU memory. During benchmarking the pre-release of the dataset, we downsampled the images by 2. However, we have found that it is beneficial to process the images in their original resolution. With the same training protocol, using images of original resolution significantly brings 1.9% and 1.8% improvements before and after CRF, respectively. In order to perform inference on this dataset with high resolution images, we split each image into overlapped regions, similar to [37]. We have also replaced the VGG-16 net with ResNet-101. We do not exploit multi-scale inputs due to the limited GPU memories at hand. Instead, we only explore (1) deeper networks (*i.e.*, ResNet-101), (2) data augmentation, (3) LargeFOV or ASPP, and (4) CRF as post processing on this dataset. We first find that employing ResNet-101 alone is better than using VGG-16 net. Employing LargeFOV brings 2.6% improvement and using ASPP further improves results by 1.2%. Adopting data augmentation and CRF as post processing brings another 0.6% and 0.4%, respectively.

Current test result: We have uploaded our best model to the evaluation server, obtaining performance of 70.4%. Note that our model is only trained on the train set.

Qualitative results: We visualize the results in Fig. 13.

4.5 Failure Modes

We further qualitatively analyze some failure modes of our best model variant on PASCAL VOC 2012 *val* set. As shown

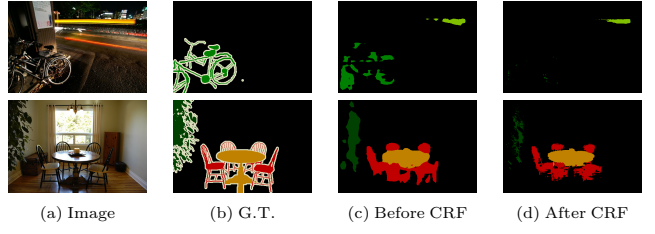


Fig. 14: Failure modes. Input image, ground-truth, and our DeepLab results before/after CRF.

in Fig. 14, our proposed model fails to capture the delicate boundaries of objects, such as bicycle and chair. The details could not even be recovered by the CRF post processing since the unary term is not confident enough. We hypothesize the encoder-decoder structure of [100], [102] may alleviate the problem by exploiting the high resolution feature maps in the decoder path. How to efficiently incorporate the method is left as a future work.

5 Conclusion

Our proposed “DeepLab” system re-purposes networks trained on image classification to the task of semantic segmentation by applying the ‘atrous convolution’ with upsampled filters for dense feature extraction. We further extend it to atrous spatial pyramid pooling, which encodes objects as well as image context at multiple scales. To produce semantically accurate predictions and detailed segmentation maps along object boundaries, we also combine ideas from deep convolutional neural networks and fully-connected conditional random fields. Our experimental results show that the proposed method significantly advances the state-of-art in several challenging datasets, including PASCAL VOC 2012 semantic image segmentation benchmark, PASCAL-Context, PASCAL-Person-Part, and Cityscapes datasets.

Acknowledgments

This work was partly supported by the ARO 62250-CS, FP7-RECONFIG, FP7-MOBOT, and H2020-ISUPPORT EU projects. We gratefully acknowledge the support of NVIDIA Corporation with the donation of GPUs used for this research.

References

- [1] Y. LeCun, L. Bottou, Y. Bengio, and P. Haffner, “Gradient-based learning applied to document recognition,” in *Proc. IEEE*, 1998.
- [2] A. Krizhevsky, I. Sutskever, and G. E. Hinton, “Imagenet classification with deep convolutional neural networks,” in *NIPS*, 2013.
- [3] P. Sermanet, D. Eigen, X. Zhang, M. Mathieu, R. Fergus, and Y. LeCun, “Overfeat: Integrated recognition, localization and detection using convolutional networks,” *arXiv:1312.6229*, 2013.
- [4] K. Simonyan and A. Zisserman, “Very deep convolutional networks for large-scale image recognition,” in *ICLR*, 2015.
- [5] C. Szegedy, W. Liu, Y. Jia, P. Sermanet, S. Reed, D. Anguelov, D. Erhan, V. Vanhoucke, and A. Rabinovich, “Going deeper with convolutions,” *arXiv:1409.4842*, 2014.
- [6] G. Papandreou, I. Kokkinos, and P.-A. Savalle, “Modeling local and global deformations in deep learning: Epitomic convolution, multiple instance learning, and sliding window detection,” in *CVPR*, 2015.

- [7] R. Girshick, J. Donahue, T. Darrell, and J. Malik, "Rich feature hierarchies for accurate object detection and semantic segmentation," in *CVPR*, 2014.
- [8] D. Erhan, C. Szegedy, A. Toshev, and D. Anguelov, "Scalable object detection using deep neural networks," in *CVPR*, 2014.
- [9] R. Girshick, "Fast r-cnn," in *ICCV*, 2015.
- [10] S. Ren, K. He, R. Girshick, and J. Sun, "Faster r-cnn: Towards real-time object detection with region proposal networks," in *NIPS*, 2015.
- [11] K. He, X. Zhang, S. Ren, and J. Sun, "Deep residual learning for image recognition," *arXiv:1512.03385*, 2015.
- [12] W. Liu, D. Anguelov, D. Erhan, C. Szegedy, and S. Reed, "SSD: Single shot multibox detector," *arXiv:1512.02325*, 2015.
- [13] M. D. Zeiler and R. Fergus, "Visualizing and understanding convolutional networks," in *ECCV*, 2014.
- [14] J. Long, E. Shelhamer, and T. Darrell, "Fully convolutional networks for semantic segmentation," in *CVPR*, 2015.
- [15] M. Holschneider, R. Kronland-Martinet, J. Morlet, and P. Tchamitchian, "A real-time algorithm for signal analysis with the help of the wavelet transform," in *Wavelets: Time-Frequency Methods and Phase Space*, 1989, pp. 289–297.
- [16] A. Giusti, D. Ciresan, J. Masci, L. Gambardella, and J. Schmidhuber, "Fast image scanning with deep max-pooling convolutional neural networks," in *ICIP*, 2013.
- [17] L.-C. Chen, Y. Yang, J. Wang, W. Xu, and A. L. Yuille, "Attention to scale: Scale-aware semantic image segmentation," in *CVPR*, 2016.
- [18] I. Kokkinos, "Pushing the boundaries of boundary detection using deep learning," in *ICLR*, 2016.
- [19] S. Lazebnik, C. Schmid, and J. Ponce, "Beyond bags of features: Spatial pyramid matching for recognizing natural scene categories," in *CVPR*, 2006.
- [20] K. He, X. Zhang, S. Ren, and J. Sun, "Spatial pyramid pooling in deep convolutional networks for visual recognition," in *ECCV*, 2014.
- [21] B. Hariharan, P. Arbeláez, R. Girshick, and J. Malik, "Hypercolumns for object segmentation and fine-grained localization," in *CVPR*, 2015.
- [22] P. Krähenbühl and V. Koltun, "Efficient inference in fully connected crfs with gaussian edge potentials," in *NIPS*, 2011.
- [23] C. Rother, V. Kolmogorov, and A. Blake, "GrabCut: Interactive foreground extraction using iterated graph cuts," in *SIGGRAPH*, 2004.
- [24] J. Shotton, J. Winn, C. Rother, and A. Criminisi, "Textonboost for image understanding: Multi-class object recognition and segmentation by jointly modeling texture, layout, and context," *IJCV*, 2009.
- [25] A. Lucchi, Y. Li, X. Boix, K. Smith, and P. Fua, "Are spatial and global constraints really necessary for segmentation?" in *ICCV*, 2011.
- [26] X. He, R. S. Zemel, and M. Carreira-Perpindn, "Multiscale conditional random fields for image labeling," in *CVPR*, 2004.
- [27] L. Ladicky, C. Russell, P. Kohli, and P. H. Torr, "Associative hierarchical crfs for object class image segmentation," in *ICCV*, 2009.
- [28] V. Lempitsky, A. Vedaldi, and A. Zisserman, "Pylon model for semantic segmentation," in *NIPS*, 2011.
- [29] A. Delong, A. Osokin, H. N. Isack, and Y. Boykov, "Fast approximate energy minimization with label costs," *IJCV*, 2012.
- [30] J. M. Gonfaus, X. Boix, J. Van de Weijer, A. D. Bagdanov, J. Serrat, and J. Gonzalez, "Harmony potentials for joint classification and segmentation," in *CVPR*, 2010.
- [31] P. Kohli, P. H. Torr *et al.*, "Robust higher order potentials for enforcing label consistency," *IJCV*, vol. 82, no. 3, pp. 302–324, 2009.
- [32] L.-C. Chen, G. Papandreou, and A. Yuille, "Learning a dictionary of shape epitomes with applications to image labeling," in *ICCV*, 2013.
- [33] P. Wang, X. Shen, Z. Lin, S. Cohen, B. Price, and A. Yuille, "Towards unified depth and semantic prediction from a single image," in *CVPR*, 2015.
- [34] M. Everingham, S. M. A. Eslami, L. V. Gool, C. K. I. Williams, J. Winn, and A. Zisserman, "The pascal visual object classes challenge – a retrospective," *IJCV*, 2014.
- [35] R. Mottaghi, X. Chen, X. Liu, N.-G. Cho, S.-W. Lee, S. Fidler, R. Urtasun, and A. Yuille, "The role of context for object detection and semantic segmentation in the wild," in *CVPR*, 2014.
- [36] X. Chen, R. Mottaghi, X. Liu, S. Fidler, R. Urtasun, and A. Yuille, "Detect what you can: Detecting and representing objects using holistic models and body parts," in *CVPR*, 2014.
- [37] M. Cordts, M. Omran, S. Ramos, T. Rehfeld, M. Enzweiler, R. Benenson, U. Franke, S. Roth, and B. Schiele, "The cityscapes dataset for semantic urban scene understanding," in *CVPR*, 2016.
- [38] L.-C. Chen, G. Papandreou, I. Kokkinos, K. Murphy, and A. L. Yuille, "Semantic image segmentation with deep convolutional nets and fully connected crfs," in *ICLR*, 2015.
- [39] C. Farabet, C. Couprie, L. Najman, and Y. LeCun, "Learning hierarchical features for scene labeling," *PAMI*, 2013.
- [40] G. Lin, C. Shen, I. Reid *et al.*, "Efficient piecewise training of deep structured models for semantic segmentation," *arXiv:1504.01013*, 2015.
- [41] Y. Jia, E. Shelhamer, J. Donahue, S. Karayev, J. Long, R. Girshick, S. Guadarrama, and T. Darrell, "Caffe: Convolutional architecture for fast feature embedding," *arXiv:1408.5093*, 2014.
- [42] Z. Tu and X. Bai, "Auto-context and its application to high-level vision tasks and 3d brain image segmentation," *IEEE Trans. Pattern Anal. Mach. Intell.*, vol. 32, no. 10, pp. 1744–1757, 2010.
- [43] J. Shotton, M. Johnson, and R. Cipolla, "Semantic texton forests for image categorization and segmentation," in *CVPR*, 2008.
- [44] B. Fulkerson, A. Vedaldi, and S. Soatto, "Class segmentation and object localization with superpixel neighborhoods," in *ICCV*, 2009.
- [45] J. Carreira, R. Caseiro, J. Batista, and C. Sminchisescu, "Semantic segmentation with second-order pooling," in *ECCV*, 2012.
- [46] J. Carreira and C. Sminchisescu, "CPMC: Automatic object segmentation using constrained parametric min-cuts," *PAMI*, vol. 34, no. 7, pp. 1312–1328, 2012.
- [47] P. Arbeláez, J. Pont-Tuset, J. T. Barron, F. Marques, and J. Malik, "Multiscale combinatorial grouping," in *CVPR*, 2014.
- [48] J. Uijlings, K. van de Sande, T. Gevers, and A. Smeulders, "Selective search for object recognition," *IJCV*, 2013.
- [49] B. Hariharan, P. Arbeláez, R. Girshick, and J. Malik, "Simultaneous detection and segmentation," in *ECCV*, 2014.
- [50] M. Mostajabi, P. Yadollahpour, and G. Shakhnarovich, "Feed-forward semantic segmentation with zoom-out features," in *CVPR*, 2015.
- [51] J. Dai, K. He, and J. Sun, "Convolutional feature masking for joint object and stuff segmentation," *arXiv:1412.1283*, 2014.
- [52] D. Eigen and R. Fergus, "Predicting depth, surface normals and semantic labels with a common multi-scale convolutional architecture," *arXiv:1411.4734*, 2014.
- [53] M. Cogswell, X. Lin, S. Purushwalkam, and D. Batra, "Combining the best of graphical models and convnets for semantic segmentation," *arXiv:1412.4313*, 2014.
- [54] D. Geiger and F. Girosi, "Parallel and deterministic algorithms from mrfs: Surface reconstruction," *PAMI*, vol. 13, no. 5, pp. 401–412, 1991.
- [55] D. Geiger and A. Yuille, "A common framework for image segmentation," *IJCV*, vol. 6, no. 3, pp. 227–243, 1991.
- [56] I. Kokkinos, R. Deriche, O. Faugeras, and P. Maragos, "Computational analysis and learning for a biologically motivated model of boundary detection," *Neurocomputing*, vol. 71, no. 10, pp. 1798–1812, 2008.
- [57] S. Bell, P. Upchurch, N. Snavely, and K. Bala, "Material recognition in the wild with the materials in context database," *arXiv:1412.0623*, 2014.
- [58] G. Papandreou, L.-C. Chen, K. Murphy, and A. L. Yuille, "Weakly- and semi-supervised learning of a dcnn for semantic image segmentation," in *ICCV*, 2015.
- [59] S. Zheng, S. Jayasumana, B. Romera-Paredes, V. Vineet, Z. Su, D. Du, C. Huang, and P. Torr, "Conditional random fields as recurrent neural networks," in *ICCV*, 2015.
- [60] J. Dai, K. He, and J. Sun, "Boxsup: Exploiting bounding boxes to supervise convolutional networks for semantic segmentation," in *ICCV*, 2015.
- [61] H. Noh, S. Hong, and B. Han, "Learning deconvolution network for semantic segmentation," in *ICCV*, 2015.

- [62] Z. Liu, X. Li, P. Luo, C. C. Loy, and X. Tang, "Semantic image segmentation via deep parsing network," in *ICCV*, 2015.
- [63] L.-C. Chen, J. T. Barron, G. Papandreou, K. Murphy, and A. L. Yuille, "Semantic image segmentation with task-specific edge detection using cnns and a discriminatively trained domain transform," in *CVPR*, 2016.
- [64] L.-C. Chen, A. Schwing, A. Yuille, and R. Urtasun, "Learning deep structured models," in *ICML*, 2015.
- [65] A. G. Schwing and R. Urtasun, "Fully connected deep structured networks," *arXiv:1503.02351*, 2015.
- [66] S. Chandra and I. Kokkinos, "Fast, exact and multi-scale inference for semantic image segmentation with deep Gaussian CRFs," *arXiv:1603.08358*, 2016.
- [67] E. S. L. Gastal and M. M. Oliveira, "Domain transform for edge-aware image and video processing," in *SIGGRAPH*, 2011.
- [68] G. Bertasius, J. Shi, and L. Torresani, "High-for-low and low-for-high: Efficient boundary detection from deep object features and its applications to high-level vision," in *ICCV*, 2015.
- [69] P. O. Pinheiro and R. Collobert, "Weakly supervised semantic segmentation with convolutional networks," *arXiv:1411.6228*, 2014.
- [70] D. Pathak, P. Krähenbühl, and T. Darrell, "Constrained convolutional neural networks for weakly supervised segmentation," 2015.
- [71] S. Hong, H. Noh, and B. Han, "Decoupled deep neural network for semi-supervised semantic segmentation," in *NIPS*, 2015.
- [72] A. Vezhnevets, V. Ferrari, and J. M. Buhmann, "Weakly supervised semantic segmentation with a multi-image model," in *ICCV*, 2011.
- [73] X. Liang, Y. Wei, X. Shen, J. Yang, L. Lin, and S. Yan, "Proposal-free network for instance-level object segmentation," *arXiv preprint arXiv:1509.02636*, 2015.
- [74] J. E. Fowler, "The redundant discrete wavelet transform and additive noise," *IEEE Signal Processing Letters*, vol. 12, no. 9, pp. 629–632, 2005.
- [75] P. P. Vaidyanathan, "Multirate digital filters, filter banks, polyphase networks, and applications: a tutorial," *Proceedings of the IEEE*, vol. 78, no. 1, pp. 56–93, 1990.
- [76] F. Yu and V. Koltun, "Multi-scale context aggregation by dilated convolutions," in *ICLR*, 2016.
- [77] J. Dai, Y. Li, K. He, and J. Sun, "R-fcn: Object detection via region-based fully convolutional networks," *arXiv:1605.06409*, 2016.
- [78] J. Dai, K. He, Y. Li, S. Ren, and J. Sun, "Instance-sensitive fully convolutional networks," *arXiv:1603.08678*, 2016.
- [79] K. Chen, J. Wang, L.-C. Chen, H. Gao, W. Xu, and R. Nevatia, "Abc-cnn: An attention based convolutional neural network for visual question answering," *arXiv:1511.05960*, 2015.
- [80] L. Sevilla-Lara, D. Sun, V. Jampani, and M. J. Black, "Optical flow with semantic segmentation and localized layers," *arXiv:1603.03911*, 2016.
- [81] Z. Wu, C. Shen, and A. van den Hengel, "High-performance semantic segmentation using very deep fully convolutional networks," *arXiv:1604.04339*, 2016.
- [82] M. J. Shensa, "The discrete wavelet transform: wedding the a trous and mallat algorithms," *Signal Processing, IEEE Transactions on*, vol. 40, no. 10, pp. 2464–2482, 1992.
- [83] M. Abadi, A. Agarwal *et al.*, "Tensorflow: Large-scale machine learning on heterogeneous distributed systems," *arXiv:1603.04467*, 2016.
- [84] A. Adams, J. Baek, and M. A. Davis, "Fast high-dimensional filtering using the permutohedral lattice," in *Eurographics*, 2010.
- [85] B. Hariharan, P. Arbeláez, L. Bourdev, S. Maji, and J. Malik, "Semantic contours from inverse detectors," in *ICCV*, 2011.
- [86] W. Liu, A. Rabinovich, and A. C. Berg, "Parsenet: Looking wider to see better," *arXiv:1506.04579*, 2015.
- [87] T.-Y. Lin *et al.*, "Microsoft COCO: Common objects in context," in *ECCV*, 2014.
- [88] R. Vemulapalli, O. Tuzel, M.-Y. Liu, and R. Chellappa, "Gaussian conditional random field network for semantic segmentation," in *CVPR*, 2016.
- [89] Z. Yan, H. Zhang, Y. Jia, T. Breuel, and Y. Yu, "Combining the best of convolutional layers and recurrent layers: A hybrid network for semantic segmentation," *arXiv:1603.04871*, 2016.
- [90] G. Ghiasi and C. C. Fowlkes, "Laplacian reconstruction and refinement for semantic segmentation," *arXiv:1605.02264*, 2016.
- [91] A. Arnab, S. Jayasumana, S. Zheng, and P. Torr, "Higher order potentials in end-to-end trainable conditional random fields," *arXiv:1511.08119*, 2015.
- [92] F. Shen and G. Zeng, "Fast semantic image segmentation with high order context and guided filtering," *arXiv:1605.04068*, 2016.
- [93] Z. Wu, C. Shen, and A. van den Hengel, "Bridging category-level and instance-level semantic image segmentation," *arXiv:1605.06885*, 2016.
- [94] K. He, X. Zhang, S. Ren, and J. Sun, "Identity mappings in deep residual networks," *arXiv:1603.05027*, 2016.
- [95] F. Xia, P. Wang, L.-C. Chen, and A. L. Yuille, "Zoom better to see clearer: Huamn part segmentation with auto zoom net," *arXiv:1511.06881*, 2015.
- [96] X. Liang, X. Shen, D. Xiang, J. Feng, L. Lin, and S. Yan, "Semantic object parsing with local-global long short-term memory," *arXiv:1511.04510*, 2015.
- [97] X. Liang, X. Shen, J. Feng, L. Lin, and S. Yan, "Semantic object parsing with graph lstm," *arXiv:1603.07063*, 2016.
- [98] J. Wang and A. Yuille, "Semantic part segmentation using compositional model combining shape and appearance," in *CVPR*, 2015.
- [99] P. Wang, X. Shen, Z. Lin, S. Cohen, B. Price, and A. Yuille, "Joint object and part segmentation using deep learned potentials," in *ICCV*, 2015.
- [100] V. Badrinarayanan, A. Kendall, and R. Cipolla, "Segnet: A deep convolutional encoder-decoder architecture for image segmentation," *arXiv:1511.00561*, 2015.
- [101] J. Uhrig, M. Cordts, U. Franke, and T. Brox, "Pixel-level encoding and depth layering for instance-level semantic labeling," *arXiv:1604.05096*, 2016.
- [102] O. Ronneberger, P. Fischer, and T. Brox, "U-net: Convolutional networks for biomedical image segmentation," in *MICCAI*, 2015.

Liang-Chieh Chen received his B.Sc. from National Chiao Tung University, Taiwan, his M.S. from the University of Michigan- Ann Arbor, and his Ph.D. from the University of California- Los Angeles. He is currently working at Google. His research interests include semantic image segmentation, probabilistic graphical models, and machine learning.



George Papandreou (S'03–M'09–SM'14) holds a Diploma (2003) and a Ph.D. (2009) in Electrical Engineering and Computer Science, both from the National Technical University of Athens (NTUA), Greece. He is currently a Research Scientist at Google, following appointments as Research Assistant Professor at the Toyota Technological Institute at Chicago (2013–2014) and Postdoctoral Research Scholar at the University of California, Los Angeles (2009–2013).



His research interests are in computer vision and machine learning, with a current emphasis on deep learning. He regularly serves as a reviewer and program committee member to the main journals and conferences in computer vision, image processing, and machine learning. He has been a co-organizer of the NIPS 2012, 2013, and 2014 Workshops on Perturbations, Optimization, and Statistics and co-editor of a book on the same topic (MIT Press, 2016).



Iasonas Kokkinos (S'02–M'06) obtained the Diploma of Engineering in 2001 and the Ph.D. Degree in 2006 from the School of Electrical and Computer Engineering of the National Technical University of Athens in Greece, and the Habilitation Degree in 2013 from Université Paris-Est. In 2006 he joined the University of California at Los Angeles as a postdoctoral scholar, and in 2008 joined as faculty the Department of Applied Mathematics of Ecole Centrale Paris (CentraleSupelec), working as an associate professor in the Center for Visual Computing of CentraleSupelec and affiliate researcher at INRIA-Saclay. In 2016 he joined University College London and Facebook Artificial Intelligence Research. His current research activity is on deep learning for computer vision, focusing in particular on structured prediction for deep learning, shape modeling, and multi-task learning architectures. He has been awarded a young researcher grant by the French National Research Agency, has served as associate editor for the Image and Vision Computing and Computer Vision and Image Understanding Journals, serves regularly as a reviewer and area chair for all major computer vision conferences and journals.



Kevin Murphy was born in Ireland, grew up in England, went to graduate school in the USA (MEng from U. Penn, PhD from UC Berkeley, Postdoc at MIT), and then became a professor at the Computer Science and Statistics Departments at the University of British Columbia in Vancouver, Canada in 2004. After getting tenure, Kevin went to Google in Mountain View, California for his sabbatical. In 2011, he converted to a full-time research scientist at Google. Kevin has published over 50 papers in refereed conferences and journals related to machine learning and graphical models. He has recently published an 1100-page textbook called “Machine Learning: a Probabilistic Perspective” (MIT Press, 2012).



Alan L. Yuille (F'09) received the BA degree in mathematics from the University of Cambridge in 1976. His PhD on theoretical physics, supervised by Prof. S.W. Hawking, was approved in 1981. He was a research scientist in the Artificial Intelligence Laboratory at MIT and the Division of Applied Sciences at Harvard University from 1982 to 1988. He served as an assistant and associate professor at Harvard until 1996. He was a senior research scientist at the Smith-Kettlewell Eye Research Institute from 1996 to 2002. He joined the University of California, Los Angeles, as a full professor with a joint appointment in statistics and psychology in 2002, and computer science in 2007. He was appointed a Bloomberg Distinguished Professor at Johns Hopkins University in January 2016. He holds a joint appointment between the Departments of Cognitive Science and Computer Science. His research interests include computational models of vision, mathematical models of cognition, and artificial intelligence and neural network